

# Injectable Microporous Annealed Particle Hydrogel Based on Guest–Host-Interlinked Polyethylene Glycol Maleimide Microgels

Adrienne E. Widener, Senthilkumar Duraivel, Thomas E. Angelini, and Edward A. Phelps\*

Microporous annealed particle (MAP) hydrogels have emerged as a versatile bio-material platform for regenerative medicine. MAP hydrogels have been used for the delivery of cells and organoids but often require annealing post-injection by an external source. An injectable, self-annealing MAP hydrogel with reversible inter-particle linkages based on guest–host functionalized polyethylene glycol-maleimide (PEG-MAL) microgels is engineered. The effect of guest–host linkages is evaluated on different types of microgels fabricated by either batch emulsion or mechanical fragmentation methods. Batch emulsion generates small spherical microgels with controllable (10–100  $\mu\text{m}$ ) diameters and mechanical fragmentation generates irregular microgels with larger diameters (100–200  $\mu\text{m}$ ). Spherical microgels (15  $\mu\text{m}$ ) show self-healing behavior and have completely recovered from high strain while fragmented microgels (133  $\mu\text{m}$ ) do not recover. Guest–host interactions significantly contribute to the mechanical properties of spherical microgels but have no effect on fragmented microgels. Spherical microgels are superior to the fragmented microgels for co-injection of immune cells and pancreatic islets due to their lower force of injection, demonstrating more homogeneously distributed cells and greater cell viability after injection. Based on these studies, the spherical guest–host MAP hydrogels provide a controllable, injectable scaffold for engineered microenvironments and cell delivery applications.

between the microgels. This interconnected interstitium promotes increased diffusion of nutrients, rapid cell migration, and vessel invasion.<sup>[7]</sup> Granular hydrogels can be made from the same polymers as bulk hydrogels and are similarly tunable for their bioactive and mechanical properties.<sup>[1,8]</sup> Furthermore, the microparticles demonstrate shear-thinning viscous behavior under applied stress that allows injection of the hydrogel.<sup>[9]</sup> These shear-thinning properties make granular hydrogel materials injectable without damage to the internal structure of the hydrogel.<sup>[6,10,11]</sup> By adding a secondary mechanism to anneal the individual micro-particles, the overall granular structure is stabilized resulting in a MAP hydrogel. However, MAP hydrogels in which the inter-particle crosslinks are covalently fixed may face challenges with injectable delivery and self-healing.<sup>[12]</sup> To address these limitations, we have engineered a class of MAP hydrogel based on reversibly interacting polyethylene glycol (PEG) hydrogel microspheres.


Methods that have been used to generate granular hydrogels include batch emul-

sion, water-in-oil microfluidics, lithography, electrohydrodynamic spraying, and mechanical fragmentation.<sup>[1,6,8,13–18]</sup> Of these methods, batch emulsion and mechanical fragmentation methods provide a quick, scalable approach to generating hydrogel microparticles. These methods result in large batches of microgels, whose sizes and polydispersity index (PDI) can be

## 1. Introduction

MAP hydrogel is a type of granular hydrogel with inter-particle bonding that has emerged as a platform for bioprinting and tissue engineering.<sup>[1–6]</sup> Granular hydrogels are composed of packed hydrogel microparticles that create a porous interstitium

A. E. Widener, T. E. Angelini, E. A. Phelps  
J. Crayton Pruitt Family Department of Biomedical Engineering  
University of Florida  
Gainesville, FL 32611, USA  
E-mail: ephelps@bme.ufl.edu

 The ORCID identification number(s) for the author(s) of this article can be found under <https://doi.org/10.1002/anbr.202200030>.

© 2022 The Authors. Advanced NanoBiomed Research published by Wiley-VCH GmbH. This is an open access article under the terms of the Creative Commons Attribution License, which permits use, distribution and reproduction in any medium, provided the original work is properly cited.

DOI: 10.1002/anbr.202200030

S. Duraivel  
Department of Materials Science and Engineering  
University of Florida  
Gainesville, FL 32611, USA

T. E. Angelini  
Department of Mechanical and Aerospace Engineering  
University of Florida  
Gainesville, FL 32611, USA

controlled by altering the time of emulsion or the time of fragmentation.<sup>[7,19]</sup> The porosity of the scaffold can be controlled by altering the size of the microgels or by changing the degree of packing through centrifugation or vacuum filtration.<sup>[16]</sup> The microporous structure creates paths of negative space surrounding the hydrogel microparticles for cells to infiltrate, migrate, spread, and proliferate.<sup>[4,11]</sup> Different fabrication methods also generate different shapes of microgels. For example, batch emulsion methods generate spherical microgels, whereas mechanical fragmentation creates irregularly shaped gels.<sup>[20]</sup>

Since granular hydrogels depend on a building-block approach to scaffold formation, different types of microgels may be mixed to form heterogeneous scaffolds. The scaffold can then be linked together using noncovalent bonding. The inclusion of these noncovalent interactions prevents microgel dispersion and structural disintegration when injected. Although microgels can be jammed together by physical interactions, adding secondary crosslinking between the individual microgels enhances stabilization under high mechanical loads.<sup>[21]</sup>

With the rising prominence of granular and MAP hydrogels used in bioprinting and for delivering cell therapies, there is a need to identify the effect of different fabrication methods on microgel size, scaffold porosity, secondary crosslinking, and viability of cellular therapies incorporated within the granular hydrogel interstitial spaces. Here, we study the effect of different batch fabrication methods of interlinked PEG-maleimide (PEG-MAL) granular hydrogels on mechanical properties and the viability of injected cells and islets. We chose PEG as a model hydrogel as one of the most common synthetic polymers used in tissue engineering. PEG is a biocompatible polymer with modular chemistry due to the addition of reactive groups (vinyl sulfone, norbornene, acrylate, or maleimide) that cap the ends of the PEG chain. Maleimide–thiol chemistry was specifically chosen for microgel generation because of its well-defined hydrogel mesh structure, stoichiometric incorporation of bioligands, increased cytocompatibility, improved cross-linking efficiency, and reaction time scales. We designed the granular hydrogel to have guest–host interactions. The host molecule  $\beta$ -cyclodextrin is a cyclic oligosaccharide of repeating D-glucose units with a hydrophobic inner core. The guest molecule, adamantane, is a hydrophobic spherical group that can reversibly crosslink with the host cyclodextrin molecule.<sup>[22,23]</sup> In the granular hydrogel scaffold, these guest–host interactions provide a noncovalent reversible crosslinking network between the individual microgels.

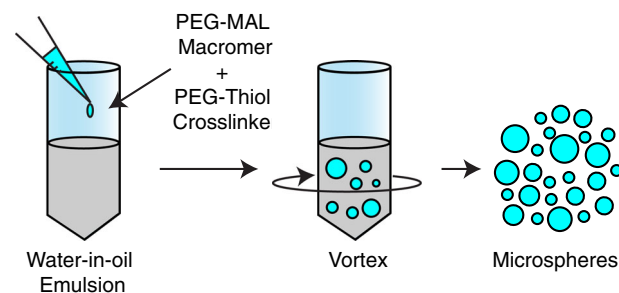
## 2. Results

We investigated batch emulsion and mechanical fragmentation as fabrication methods to generate granular hydrogels with and without guest–host interparticle interactions. Synthesis of guest–host hydrogel precursor molecules was performed to conjugate adamantane–thiol and mono-6-mercapto- $\beta$ -cyclodextrin to 4-arm PEG-MAL chains before crosslinking. The functionalized macromers were then mixed with a stoichiometrically balanced amount of 4-arm PEG-thiol (PEG-SH) crosslinker at pH 5.4 and a trace amount of Alexa Fluor-MAL for visualization. The number of PEG arms between the PEG-MAL macromer and the PEG-SH crosslinker were matched to reduce the incidence of

intramolecular primary loops within the hydrogel structure.<sup>[24]</sup> For the batch emulsion method, this mixture was immediately vortexed in mineral oil to generate an emulsion and allowed to finish crosslinking on a rocker for 30 min. The microgels were then collected by centrifugation and washed (Figure 1A). For mechanically fragmented microgels, guest–host-functionalized bulk PEG-MAL gels were cast in a 24-well plate and homogenized in deionized water with a tissue homogenizer (Figure 1B).

We compared the particle and pore size of the microspheres and fragmented gels by adding high molecular weight TRITC dextran to fill the void space between the individual hydrogel microparticles and imaging by confocal microscopy (Figure 2A,B). We found that the diameter of the microspheres made by a 30 s vortex time was on average smaller than the fragmented gels made at 4 min homogenization time (Microspheres:  $\langle D \rangle = 14.8 \mu\text{m}$ , PDI = 0.22, Fragmented Gels:  $\langle D \rangle = 132.6 \mu\text{m}$ , PDI = 0.31). (Figure 2C). We determined that the PDI decreased with decreasing size of the microsphere but did not decrease with the size of the fragmented bulk gels. Through the emulsion method, we were able to control the size of the microspheres based on the vortexing time ranging from 15 to 90 s (Figure 2D). We studied the effect of increasing the homogenization time of the initial bulk gel to generate smaller fragmented gels from 1 to 5 min in 1 min intervals but were unable to significantly change the size of the particles based on homogenization time (Figure 2E). The average interparticle distance between the fragmented gels ( $36.63 \mu\text{m}$ )

### A Batch Emulsion



### B Mechanical Fragmentation

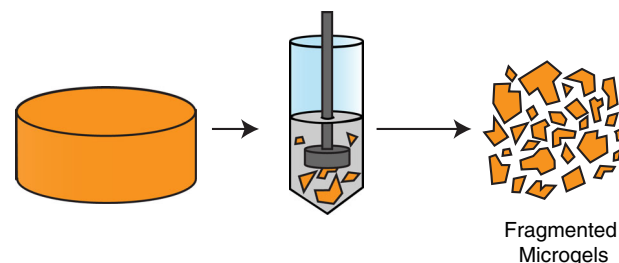


**Figure 1.** Fabrication methods of granular hydrogels. A) Batch water-in-oil emulsion fabrication of PEG-MAL granular hydrogels. 4-arm PEG-MAL macromer and 4-arm PEG-SH crosslinker at pH 5.4 is added into a mineral oil and surfactant solution and quickly vortexed for 30 s while crosslinking occurs. Microspheres are isolated using centrifugation and washed to remove excess oils. B) Mechanical fragmentation of bulk 4-arm PEG-MAL hydrogels. The bulk gel is minced, added to a volume of DI water, and fragmented for 4 min using a 20 mm tissue homogenizer. Fragmented gels are isolated by centrifugation.

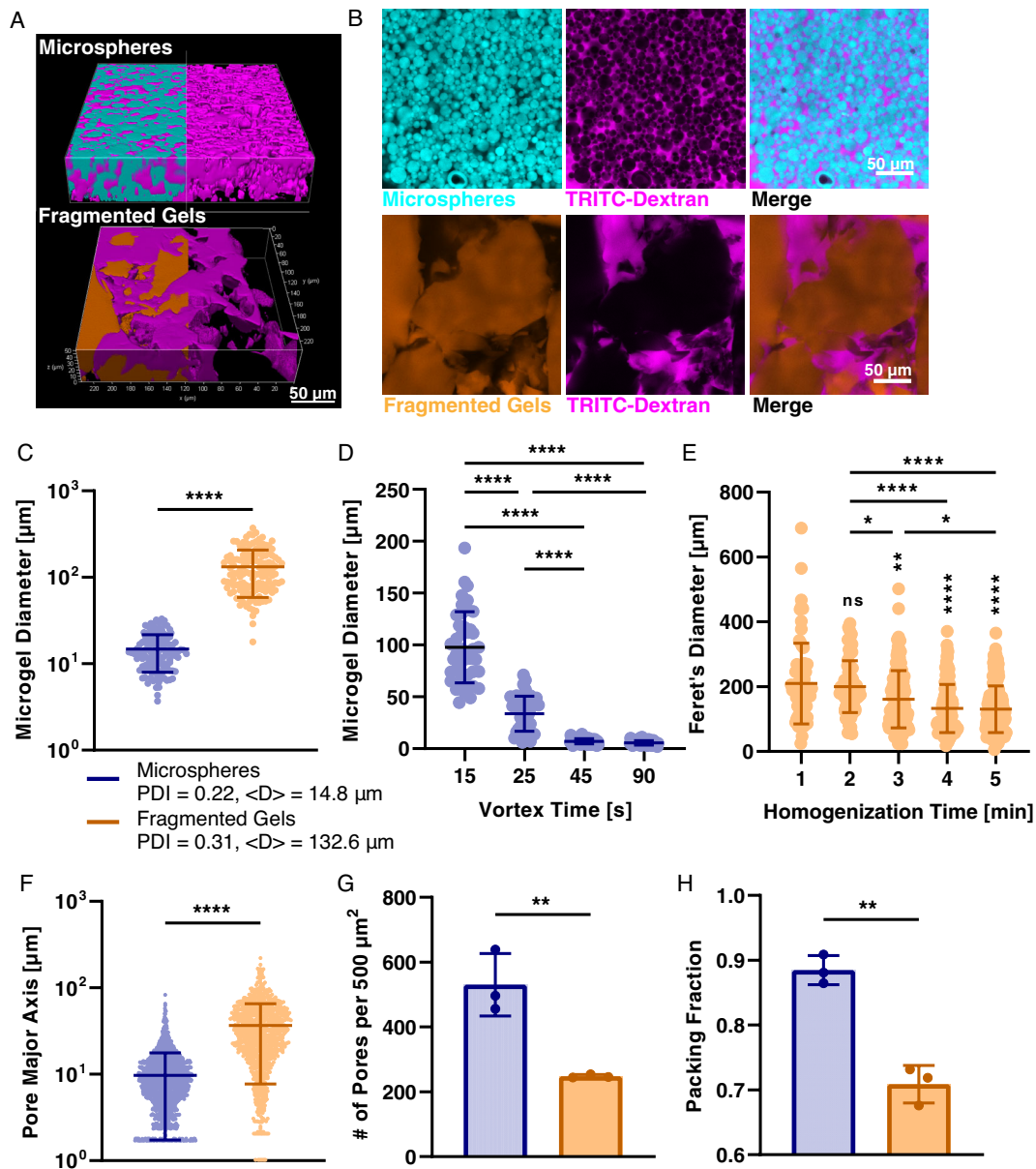


**Figure 2.** Particle and pore size analysis of granular hydrogels. A) 3D-rendered confocal images of Alexa Fluor-MAL-488 labeled microspheres (cyan) and fragmented gels (orange) incubated with high molecular weight TRITC-dextran (magenta). B) Confocal images of microspheres and fragmented gels with TRITC-dextran infiltration and merge. C) Microgel diameter for microspheres (30 s) and fragmented gels (4 min). Microgel diameter of fragmented gels is greater than microspheres and the polydispersity index is much higher for fragmented gels. D) Demonstration of the control over the size of the microsphere through alteration of vortex time from 15 to 90 s. E) Lack of control over the size of fragmented gels through mechanical fragmentation from 1 min homogenization to 5 min. Significance from 1 min time group displayed above groups, all other comparisons are displayed as bars above all groups. F) Interparticle distance between pores of scaffold for microspheres and fragmented gels as measured by the major axis of each pore. G) The number of pores per area for both microspheres and fragmented gels. H) The packing fraction of microspheres and fragmented gels. For all panels, significance between means of three or more groups was determined by one-way analysis of variance (ANOVA),  $p < 0.05$  with Tukey's posthoc pairwise comparisons, and significance between means of two groups was determined by two-tailed student's *t*-test. \* =  $p < 0.05$ , \*\* =  $p < 0.01$ , \*\*\*\* =  $p < 0.0001$ , \*\*\*\* =  $p < 0.0001$ .

was significantly greater than that of the microspheres (9.7  $\mu\text{m}$ ) (Figure 2F). The number of pores within a  $500 \mu\text{m}^2$  area was significantly higher for microspheres (530 pores) than for fragmented gels (248 pores) (Figure 2G), and the resulting packing fraction of the microspheres was significantly higher than the fragmented gels (Figure 2H). Based on the size of the particles

and resultant pore sizes we found that we had greater control over the batch emulsion method compared to the mechanical fragmentation method. This control allows for the tailoring of the scaffold to mimic the interstitial architecture of specific tissues and control the pore size for cell invasion and migration within the scaffold.

We next characterized the effect of the guest–host interactions on the mechanical properties of packed microspheres and fragmented gels through a series of rheological tests. Guest–host scaffolds were formed by adding equal volumes of  $\beta$ -cyclodextrin and adamantane functionalized granular hydrogels to a suspension and packing by centrifugal filtration. Guest–host scaffolds were compared to scaffolds composed only of host microgels (host–host). We performed a low amplitude (1%) oscillatory frequency sweep from 10 to 0.01 Hz. Both the guest–host fragmented gels and the guest–host microspheres demonstrated viscoelastic behavior (Figure 3A), with a frequency-independent storage modulus ( $G'$ ) greater than the loss modulus ( $G''$ ) over the range of the frequency sweep. Guest–host fragmented gels had a similar storage modulus at 1 Hz (1860 Pa) to the guest–host microspheres (1840 Pa). The storage modulus of the host–host fragmented gels was significantly higher than the host–host-microspheres (host–host-fragmented gels = 2050 Pa, host–host-microspheres = 670 Pa) (Figure 3B).

We conducted an oscillatory strain sweep from 0.01 to 500% at a constant frequency of 1 Hz and determined the approximate yield stress and for all groups (Figure 3C,D). For guest–host functionalized microgels, there was no significant difference in the approximate strain rate amplitudes and resulting yield stress between microspheres (430 Pa) and fragmented gels (550 Pa). However, for host–host microgels, there was a significant difference between the strain rate amplitude and resulting yield stress of microspheres (120 Pa) and fragmented gels (700 Pa) (Figure S1A,B, Supporting Information). We compared the storage modulus at 1 Hz between the guest–host and host–host functionalized groups to determine the effect of guest–host interactions on the different granular hydrogels. We found that storage modulus at 1 Hz was significantly different between the guest–host and host–host microspheres, but that guest–host functionalization had no effect on this measurement for the fragmented gels (Figure 3E).

Next, we performed a cyclic strain sweep alternating between low (1%) and high (500%) strains to understand the shear-thinning and recovery characteristics of the granular hydrogels (Figure 3F,G). The guest–host and host–host microspheres were able to recover their initial storage modulus after both periods of high strain, whereas both the guest–host and host–host fragmented gels had a decrease in their storage modulus (Figure 3H). We conducted a unidirectional shear rate sweep to investigate how guest–host interactions influenced the yielding and shear-thinning of packed microspheres and fragmented gels (Figure 3I,J). All materials demonstrated a shear-thinning behavior with decreasing viscosity as the shear rate increased. We determined the yield stress of the materials using linear regression of the flow curves for guest–host microspheres (190 Pa), guest–host fragmented gels (670 Pa), host–host microspheres (120 Pa), and host–host fragmented gels (620 Pa). We then compared this to the yield stress calculated from the strain sweep experiments (Figure 3C,D) and plotted them to compare the yield stresses (Figure 3K). We found that the microspheres without guest–host interactions had the lowest yield stress, followed by the microspheres with guest–host interactions, and then the two fragmented gel groups which had very similar yield stresses. We note that the shear rate sweeps shown in Figure 3I,J do not exhibit the characteristic upturn in shear stress at high

shear rates that granular gels typically exhibit.<sup>[25]</sup> We hypothesized that the crossover shear rate to a fluid-like state occurred at a higher shear rate than tested with the unidirectional shear rate sweep. To test this hypothesis, we performed a strain-rate frequency superposition (SRFS) analysis on the oscillatory strain sweep to determine the shear rate at yielding. SRFS is performed by mapping the strain amplitude at a given frequency to the strain rate. We found that the crossover shear rates were more than an order of magnitude higher than the largest shear rate tested in the unidirectional sweeps (Figure S1C, Supporting Information). These results indicate that the apparent stress plateau in the unidirectional shear rate sweep corresponds to the yield stress. (Figure S1C, Supporting Information).<sup>[26]</sup>

Based on our rheological analysis, we found that there were no significant differences between the fragmented gels with and without guest–host interactions. Our initial hypothesis was that the fragmented gels would have increased availability for guest–host interactions due to the larger surface areas between the individual gels. However, the force of friction caused by the anisotropy of the particles poses a greater force than the combined guest–host interactions between the particles. This is seen in the ability to maintain the same modulus in the frequency sweeps (Figure 3A,B), in the lack of self-healing (Figure 3F, G), and in the higher yield stress across both unidirectional and oscillatory sweeps (Figure 3K). However, the guest–host interaction is prominent in the behavior of spherical microgels, which have a higher packing fraction.

Next, we investigated the use of the granular hydrogels as an injectable cell and islet delivery scaffold due to their shear-thinning and self-healing properties. To characterize the injectability of the hydrogel microparticles, we measured the extrusion force of our guest–host microspheres and fragmented gels through a 20G, 1" needle (Figure 4A). Microgels with guest–host interactions had a significantly higher extrusion force than their host–host counterparts. Further, the guest–host fragmented gels had a significantly higher extrusion force than the guest–host microspheres (Figure 4B). We used this data in combination with our previous rheological analysis to derive the wall shear stress within the needle for each material (Supporting Information). We found that the wall shear stress of the microgels was significantly higher than the 1X PBS control (Figure 4C). The maximum shear stress for all groups was of a similar order to the physiological shear stress within microvasculature ( $\approx 9.5$  Pa).<sup>[27]</sup> When injected, the microspheres and fragmented gels underwent a partially laminar flow at the edges of the needle and a plug flow in the center of the needle, this is representative of the turbulent flow for a Herschel–Bulkley fluid, a non-Newtonian fluid with a power law index and yield stress.<sup>[28,29]</sup>

To investigate cytocompatibility during injection under high shear stresses, we loaded the microspheres and fragmented gels with Jurkat T cells by mixing the cells and microgels in a suspension, packing the scaffold down by centrifugation, and loading them into a 1 mL syringe. We injected a total of 150  $\mu$ L of microspheres and fragmented gels loaded with Jurkat T Cells into a rectangular channel (Ibidi  $\mu$ slide VI 0.4) and labeled the cells with Calcein AM and ethidium-homodimer-1 (EthD-1) to visualize the distribution and viability of cells within the scaffold after injection (Figure 5A). The first 50  $\mu$ L injected from the syringe contained few microspheres or fragmented gels and contained

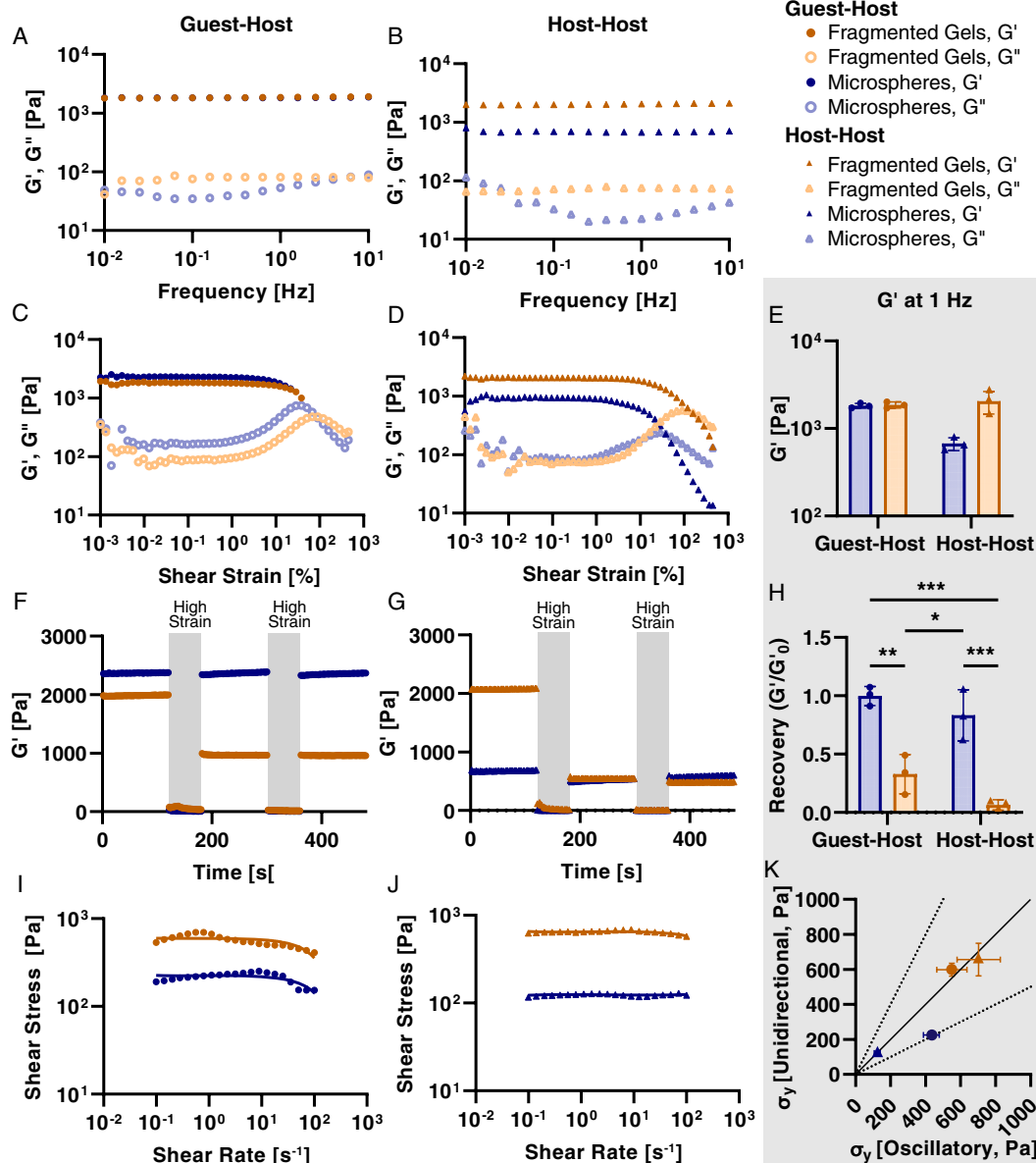


**Figure 3.** Rheology of granular hydrogels. Frequency sweeps from 10 to 0.01 Hz at 1% amplitude for: A) guest–host microspheres and fragmented gels and B) host–host microspheres and fragmented gels. All gels demonstrate viscoelastic behavior over the frequency range. Strain sweep from 100 to 0.001% shear strain for: C) guest–host microspheres (blue, circle) and fragmented gels (orange, circle) and D) host–host microspheres (blue, triangle) and fragmented gels (orange, triangle). E) Storage modulus at 1 Hz for guest–host and host–host microspheres and fragmented gels. Cyclic strain alternating between low (1%) and high (500%) strain over 60 s for: F) guest–host and G) host–host gels. The high strain region is indicated by a gray overlay. H) The recovery ( $G'/G'_0$ ) of the initial and final storage modulus in the cyclic strain experiment (F,G). I,,J) Shear-thinning was identified in both the microsphere and fragmented microgels via a unidirectional shear rate sweep. The solid lines indicate the linear regression at the zero-frequency limit. The curvature was determined to be due to the time-dependent nature of reconstruction within the material. Yielding was not observed in this shear rate domain, as determined by the yield strain rate in the oscillatory strain sweeps (Figure 3C,D, and S1, Supporting Information). K) The calculated yield stress from the unidirectional shear rate sweeps and the oscillatory shear strain sweeps comparison. All groups fall within the 1:1 correlation except for the guest–host microspheres which are still within the twofold range. For all panels, significance between means of three or more groups determined by one-way ANOVA,  $p < 0.05$  with Tukey's post-hoc pairwise comparisons. \*\* =  $p < 0.01$ , \*\*\* =  $p < 0.001$ , \*\*\*\* =  $p < 0.0001$ .

an abundance of cells. The microspheres began flowing in the next 50–100  $\mu\text{L}$ , while the fragmented gels did not flow until the final 100–150  $\mu\text{L}$  of the injected volume (Figure 5B,C). We found that the interstitial fluid is eluted first and flowed around

the microgels packed into the syringe along with most of the cells within the media before the yielding of the microgels in the latter fractions of the injection. These results demonstrate granular convection and separation of the microgels and cells during

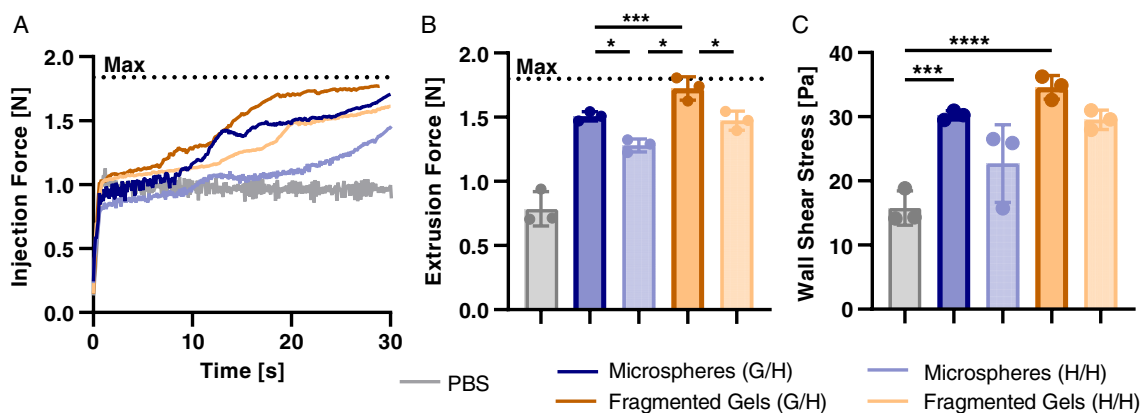


**Figure 4.** Injectability of granular hydrogels. A) The injection force of guest–host and host–host microspheres and fragmented gels, and 1X PBS as measured by a force sensor in a 1 mL syringe with a 20G, 1" needle. The maximum force that the force sensor could measure is indicated by the dashed line. B) The maximum extrusion force was calculated from the injection force experiment. C) Wall shear stress calculated from the derived Navier–Stokes equations. For all panels, significance between means of three or more groups determined by one-way ANOVA,  $p < 0.05$  with Tukey's posthoc pairwise comparisons. \* =  $p < 0.05$ , \*\* =  $p < 0.01$ , \*\*\* =  $p < 0.001$ , \*\*\*\* =  $p < 0.0001$ .

the injection. The fragmented gels were unable to maintain a consistent cell distribution during the injection. Further, although the distribution of cells in the microspheres was not perfect within the microsphere scaffold, there is more predictability of the presence of cells within all parts of the injection. Cells injected within the microsphere scaffold showed greater viability in all phases of the injection, whereas those injected in the fragmented gels had lower viability (Figure 5D). The lower viability of cells injected in fragmented gels may be due to the increased extrusion force and shear surfaces between fragmented gels (Figure 4B).

We engineered these self-healing MAP hydrogels as a vehicle for cell delivery, where vasculature and immune cells can rapidly infiltrate the interior of the scaffold to integrate transplanted cells or organoids with host systems. To begin to understand how these materials function as a vehicle for injectable cell delivery, we assessed the viability of human pancreatic islets co-injected with the fragmented and microsphere scaffolds. Human islets were loaded with either guest–host microspheres or fragmented gels into the back of a syringe, injected, and stained for viability. Islets injected with spherical microspheres showed no change in viability from no injection control islets or islets injected in media, while islets injected with fragmented gels were significantly less viable (Figure 6A,B).

### 3. Discussion

Here we investigated the mechanical and biophysical properties of granular hydrogels for injectability and cell and islet delivery. Previously, we have shown the benefit of using granular hydrogels for rapid cell migration and created spherical microgels with shear-thinning capabilities.<sup>[7]</sup> We further expanded on our understanding of self-healing MAP hydrogel to demonstrate the contribution of guest–host molecules to mechanical properties and investigate different fabrication methods.

Two types of granular hydrogels were formed by either batch emulsion or mechanical fragmentation. Both methods generated

large quantities of PEG-MAL microgels without the need for large parallelization of microfluidic devices. We found that we could not control the average size of mechanically fragmented gels by altering the time of homogenization and compared that to our previous findings of controlling the size of microspheres made by batch emulsion. The batch emulsion method resulted in on average smaller microgel sizes (14.8  $\mu\text{m}$ ), whereas mechanical fragmentation was limited to microgels of larger sizes (132.6  $\mu\text{m}$ ) (Figure 2C). By controlling the size of the microgels, we could change the resulting pore size of the scaffold. The particle and pore size of the scaffold has been shown to influence cell invasion and migration through the scaffold and inflammatory response.<sup>[30]</sup>

We attempted to make fragmented gels of smaller sizes using both smaller rotor-stator generator probes and sieving to separate particle sizes but were unable to generate smaller gels. Rotor stators are high shear mixers that incorporate both a rotor and a stationary stator. As the rotor turns at high speeds within the stationary stator, it creates a vortex circulating the product through the gap between the rotor and stator, mechanically shearing the contents at high speeds and creating a very homogenous blend. We found that there was a fragmented particle size limit (around 100  $\mu\text{m}$ ) reached when the shear forces applied by the homogenizer could no longer surpass the ultimate tensile strength of the hydrogel. The relationship among the hydrogel ultimate tensile strength, shear force, and particle size has been systematically investigated by others for pectin and agarose gels.<sup>[31,32]</sup> They show that particle size is dictated by the balance between shear force and ultimate tensile strength. This explains why smaller microgels were only able to be generated by emulsion: the shear force is applied before the hydrogel has completed crosslinking. In our engineering design criteria, we wanted to make microgels of  $\approx 20 \mu\text{m}$  in diameter such that the interstitium of the MAP constructs would mimic the length scales of the native pancreatic architecture. This criterion was achievable using the batch emulsion method, but not mechanical fragmentation by homogenization. Future methods to create smaller fragmented

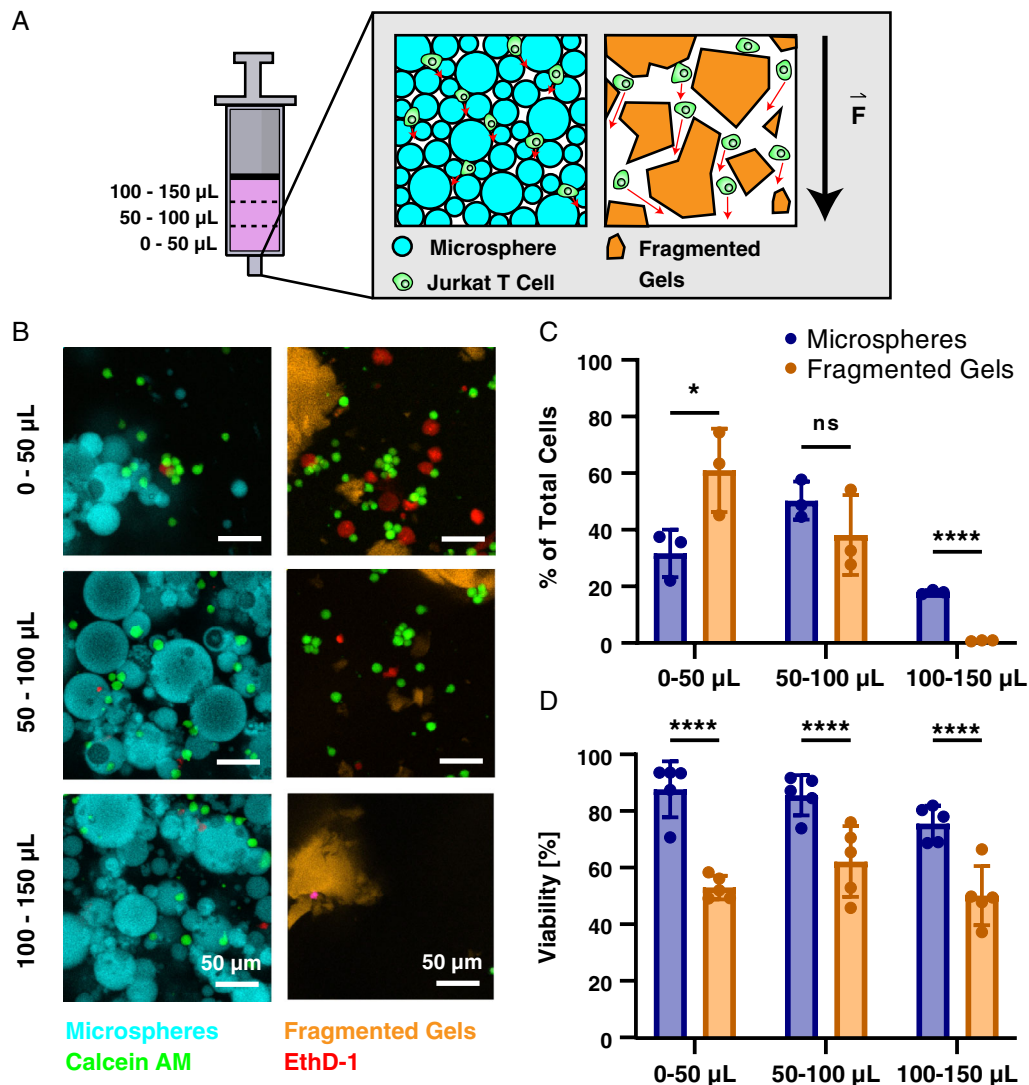


**Figure 5.** Distribution and viability of cells injected within granular hydrogels. A) Graphical representation of the experiment. Syringes were loaded with microspheres or fragmented gels loaded with Jurkat T Cells and injected into a dish. The injection was partitioned into 50  $\mu\text{L}$  volumes for a total of 150  $\mu\text{L}$  and each eluted fraction was imaged to quantify the distribution of cells and microspheres. Graphical representations of granular convection of cells and MAP scaffold as force is being applied during injection. The cells within the microspheres have shorter elution paths (represented by a red arrow) than cells within the fragmented gels due to the higher packing of microspheres. The cells within the fragmented gels have more space to elute around the gels due to the larger sizes of the particles. The black arrow represents the force applied during the injection. B) Confocal images of the injection fractions. In the first 50  $\mu\text{L}$  of injection, the cells elute around the microspheres and fragmented gels. During the next 50  $\mu\text{L}$  (50–100), the microspheres yield and contain the cells in the interstitial spaces between the gels. In the last 100–150  $\mu\text{L}$  the fragmented gels begin to flow but lack cells as most have moved past the large particles in the first 100  $\mu\text{L}$  of injection. C) Quantification of the percent of total cells per  $\mu\text{L}$  of injection for microspheres and fragmented gels in each fraction of the injection. D) Percent viability of total cells injected in each stage of injection. For all panels, significance was determined by two-tailed student's *t*-tests between the microsphere and fragmented group at each stage of the injection. \* =  $p < 0.05$ , \*\* =  $p < 0.01$ , \*\*\* =  $p < 0.001$ , \*\*\*\* =  $p < 0.0001$ .

gels may include extrusion fragmentation, cryogenic grinding (cryomilling), or blending.<sup>[33–35]</sup>

We hypothesized that guest–host interactions on the fragmented gels would have a greater influence on the mechanical properties of the scaffold due to the larger surface interactions between the individual microgels. These larger surface areas could provide more guest–host interactions and create a greater cumulative interaction. We tested this hypothesis by conducting

a series of rheological studies between guest–host functionalized gels and host–host-functionalized gels to control for crosslinking density of the hydrogel. In a frequency sweep from 100 to 0.01 Hz we found that both spherical and fragmented guest–host granular hydrogel scaffolds showed viscoelastic behavior (Figure 3A). When comparing the storage modulus at 1 Hz there was no statistical difference between the two types of gel (Figure 3E). We found that the addition of guest–host

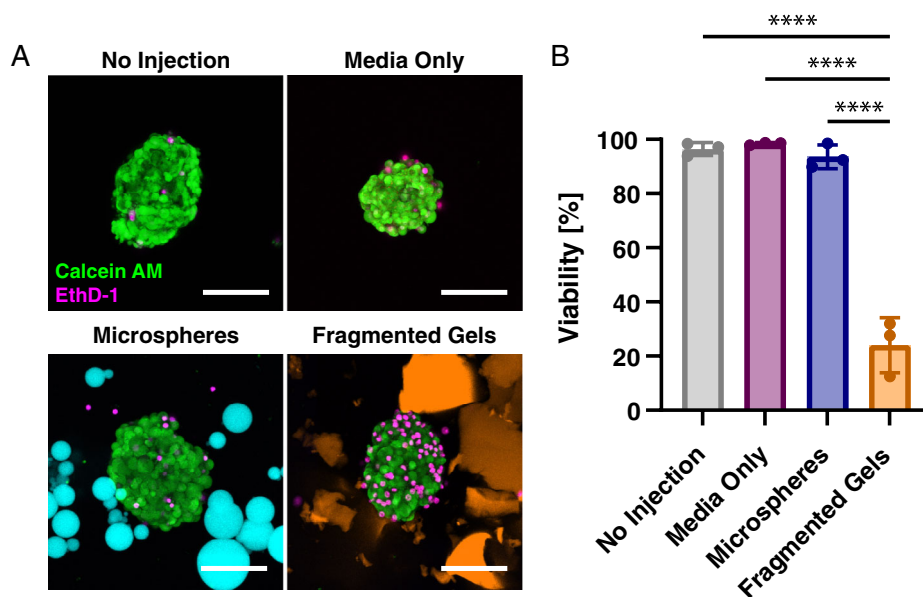


**Figure 6.** Injection of islets within granular hydrogels. A) Human pancreatic islets injected in microspheres (cyan), fragmented gels (orange), media only as compared to a no-injection control. Islets were stained with Calcein AM (Live, green) and EthD-1 (dead, red) after injection, and PEG-MAL gels are labeled with Alexa Fluor-MAL-647. Media was added to dilute and disperse the microspheres and fragmented gels after injection to aid in identifying and imaging islets. Scale bar is 50  $\mu\text{m}$ . B) Percent viability of the islets after injection within media-only, microspheres, fragmented gels, as compared to a no-injection control. Percent viability was calculated by dividing the number of live cells by the total number of cells in the islet, data is representative of multiple donors. Significance between means of three or more groups determined by one-way ANOVA,  $p < 0.05$  with Tukey's post-hoc pairwise comparisons. \* =  $p < 0.05$ , \*\* =  $p < 0.01$ , \*\*\* =  $p < 0.001$ , \*\*\*\* =  $p < 0.0001$ .

interactions to the spherical microgels increased the storage modulus by 1 Hz by 1.8-fold, while the addition of guest–host interactions had no effect on the storage modulus of irregular fragmented microgels. These results were contrary to our original hypothesis that guest–host interactions would have a greater effect on the mechanical properties of irregular microgels. We speculate that this is due to the influence of high local frictional forces between the irregular-shaped microgels making the guest–host interactions negligible in magnitude.

In previous studies, granular hydrogels have shown to be a shear-thinning injectable material.<sup>[7,10,36–38]</sup> We compared the shear-thinning and self-healing properties of the different fabrication methods by conducting a cyclic strain experiment between 1% and 500% strain to simulate injection conditions. Both fabrication methods demonstrated a shear-thinning hydrogel; however, the microspheres had significantly increased self-healing capabilities. The percent difference in the initial and final storage modulus following high strain demonstrates the ability of the spherical guest–host gel formulation to better recover its original mechanical properties (Figure 3F,G). The lower local frictional forces between the microspheres than the fragmented gels which have more angularity between the particles may have prevented the fragmented gels from recovering.<sup>[39]</sup> The spherical microgel scaffold can more easily rearrange and return to the original modulus because there is more slip between individual microgels. The self-healing behavior is increased with the presence of guest–host interactions in microspheres, stabilizing the structure after the strain is removed. In the fragmented gels, the guest–host interactions did not have a significant effect on

the self-healing capabilities of the material as local frictional forces cause granular networks to be less connected and more anisotropic.<sup>[39]</sup>

We sought to understand the injectability of the granular hydrogels and the viability of injected cells and islets. We loaded syringes with spherical or irregular microgels and measured the force of injection applied to the syringe by a syringe pump. We measured the peak injection force and derived the ejection pressure for each group. Guest–host fragmented gels had the highest extrusion force followed by host–host fragmented gels and the guest–host microspheres. Different from the rheology results, the addition of guest–host interactions had similar effects on both the microspheres and fragmented gels by increasing the force of extrusion. To further elucidate the effects of the shape of the microgels and the guest–host interactions, we derived the wall shear stress within the needle for each of the groups to determine the maximum stress applied to the cells during injection. We found that there were no significant differences in the wall shear stress between the groups of microgels, possibly due to the complex behavior of viscous granular flows through circular pipes with a turbulent flow that is not captured in our derivation of the Navier–Stokes equations (Supporting Information). Future studies including computational fluid dynamics are currently being carried out to investigate this phenomenon.

To inject homogeneous constructs, the location of cells and organoids within the scaffold must be controllable. We determined the distribution of cells loaded into the scaffolds by loading each of the microsphere and fragmented gel scaffolds with Jurkat T cells and injecting them into a channel slide for



visualization. Cells injected with the microspheres were more evenly distributed in the extruded volume than cells in irregular fragmented microgels. We found that microspheres with a lower yield stress (Figure 3K) were able to flow more quickly and under a smaller stress than the fragmented gels. During injection, we observed granular convection within the granular hydrogel structure. Incorporated cells elute and flow out from the syringe and around the microgels before the yielding and elution of the particles themselves (Figure 5A). Granular separation during injection also occurs in the spherical microgels, but to a lesser extent due to the tighter packing structure. The high packing density of the microgels led to a more even distribution of the cells throughout the scaffold across all volumes extruded.

Finally, we assessed the viability of human islets co-injected with the microsphere or fragmented gel scaffolds. We mixed islets within the granular hydrogels, loaded them into syringes, injected them into a petri dish, and stained them for viability to understand the effect of injection forces on the viability of the islets. We found that islets injected with the microspheres had significantly higher viability than the islets injected within the fragmented gels. Microspheres provided a better environment for the islets during injection because of the lower frictional forces between the particles allowing for a lower yield stress and flow to occur. Since the fragmented gels had greater forces of friction between the particles, the islets embedded within the scaffold likely experienced greater shear forces due to the particle-to-particle interactions.

## 4. Conclusion

In this study, we investigated two different batch methods of microgel fabrication for generating MAP hydrogel scaffolds. We demonstrated that smaller spherical microgels provided superior injectability and self-healing capabilities over larger fragmented gels. Guest–host interactions on the granular hydrogels provided self-healing capabilities for spherical microgels. By encapsulating cells and islets within the interstitial spaces, we show that granular hydrogels made by a batch emulsion method are a quick and effective way to generate an injectable, shear-thinning scaffold safe for cell and islet delivery. Future studies include the use of spherical granular hydrogels in the delivery of islets for the treatment of type 1 diabetes.

## 5. Experimental Section

**Chemicals and Reagents:** 4-arm PEG-MAL (20 kDa) was purchased from Laysan Bio. 4-arm PEG-SH (20 kDa) was purchased from Jenkem Technology. 1-adamantane-thiol, Span 80, mineral oil, TRITC-Dextran (500 kDa), and triton-X 100 were obtained from Sigma Aldrich. Mono(6-mercapto-6-deoxy)- $\beta$ -cyclodextrin was obtained from Zhiyuan Biotechnology.

**Microsphere Synthesis:** PEG-MAL (4-arm, 20 kDa) (120 mg mL<sup>-1</sup>, 5 mM) macromer was dissolved in phosphate-buffered saline (PBS) with 1% HEPES at pH 5.4 and split into two equal volumes. The reduced pH helps to slow down the crosslinking reaction, which proceeds so quickly at neutral pH as to hinder mixing and handling.<sup>[40]</sup> At pH 5.4, gelation of PEG-MAL with PEG-SH takes, on average, 34 s.<sup>[7]</sup> 1-Adamantane-thiol was dissolved in dimethyl sulfoxide (DMSO) (1.8 mg mL<sup>-1</sup>, 1 mM) and mono-6-mercapto- $\beta$ -cyclodextrin was dissolved in 1X PBS with 1% HEPES at pH 5.4 (122 mg mL<sup>-1</sup>, 1 mM). Adamantane-thiol and

mono-thiol- $\beta$ -cyclodextrin were added dropwise to each of the PEG-MAL solutions at a 1:1 molar ratio and reacted for 30 min at room temperature to functionalize 1 of the 4 PEG-MAL arms with guest or host molecules. PEG-SH (4-arm, 20 kDa) (82.2 mg mL<sup>-1</sup>, 8 mM) was dissolved in PBS with 1% HEPES at pH 5.4 and reacted with a trace amount of Alexa Fluor-MAL for 5 min to aid in microgel visualization. PEG-SH was added to PEG-MAL at a 1:1 volume ratio, quickly pipetted up and down several times to mix thoroughly, then transferred to a 30 $\times$  volume of mineral oil with 2% vol/vol Span 80 surfactant in a 50 mL conical tube. The tube was vortexed for 30 s to generate an emulsion, then allowed to finish cross-linking for 30 min at 25 °C on a rocker plate to generate microgels of final polymer concentration of 10% wt/vol. Crosslinked microgels were centrifuged at 3,000  $\times$  g for 5 min and washed three times with 0.3% Triton X-100 in deionized (DI) water, once with 50% acetone in DI water, once with DI water, and finally once with PBS at pH 7.2. The microgels were then packed together by centrifugal filtration using Costar 0.45  $\mu$ m microcentrifuge filters at 3,000  $\times$  g for 10 min. Granular gels were formed by adding equal weights of adamantane-microgels and  $\beta$ -cyclodextrin-microgels to a centrifuge tube, suspending in PBS, vortexed for 30 min, and packed by centrifugal filtration as described above.

**Fragmented Gel Synthesis:** PEG-MAL macromer (120 mg mL<sup>-1</sup>) functionalized with adamantane or  $\beta$ -cyclodextrin and labeled with trace amounts of Alexa Fluor-MAL-568 and Alexa Fluor-MAL-488 was cross-linked for 30 min at 25 °C in a 12 well plate. After crosslinking, bulk gels were minced using a razor blade and added to 5 mL of DI water in a 15 mL conical tube. The gels were fragmented using a Pro Scientific tissue homogenizer with a 20 mm generator probe for 4 min. Networks were formed by adding equal amounts of adamantane-fragmented microgels and  $\beta$ -cyclodextrin-fragmented microgels to a centrifuge tube and vortexing for 30 min. They were then packed together by centrifugal filtration using a Costar 0.45  $\mu$ m microcentrifuge filter at 3,000  $\times$  g for 10 min.

**Particle and Pore Size Analysis:** Microsphere size distribution and guest–host interactions were characterized by confocal microscopy. Microsphere diameters were quantified directly using the Analyze Particles plugin for the Fiji distribution of ImageJ.<sup>[41]</sup> For fragmented microgels, a Gaussian filter was first applied, the images were binarized, a watershed filter was applied, and the particles were then analyzed using the Analyze Particles plugin for Fiji.<sup>[41]</sup> Regions of interest (ROIs) were manually adjusted to correct for any error in the watershed analysis. The major axis was taken as the Feret's diameter of the particle. The particle size data were then analyzed by frequency distribution with a bin size of 5, and the average diameter and standard deviation were used to determine the PDI (Equation (1)), where  $\sigma$  is the standard deviation and  $\langle D \rangle$  is the average diameter.<sup>[42]</sup>

$$\text{Polydispersity Index (PDI)} = \left( \frac{\sigma}{\langle D \rangle} \right)^2 \quad (1)$$

Pore size analysis was determined by incubating the assembled microgel scaffold with high molecular weight TRITC-Dextran (500 kDa) for 1 h and then imaged using confocal microscopy. The high molecular weight prevents dextran from diffusing into the microgels and instead labels the pores around the individual microgels. A Gaussian filter was applied, images were binarized, a watershed filter was applied, and the particles were analyzed using the Analyze Particles plugin for Fiji.<sup>[41]</sup> The area and major axis lengths for each pore were then averaged across each condition. The packing fraction for each condition was determined by dividing the cross-sectional area of the labeled pores by the cross-sectional area of the total gel volume imaged.

**Rheological Measurements:** Rheological measurements were performed on an Anton Paar MCR 702 Rheometer with a 20 mm roughened plate on plate configuration with a 0.5 mm gap height at 25 °C. To prepare samples for rheology, the samples were first loaded into a 0.45  $\mu$ m Costar centrifuge filter tube and centrifuged at 3,000  $\times$  g for 5 min to remove any excess water and pack gels. To load the samples, about 1 mL of the microgels were placed on the bottom plate at room temperature. Oscillatory shear strain amplitude sweeps were performed at 1 Hz between strains of 0.01% and 500%. Yield stress and strain were determined by taking the second

derivative of the fitted curve and finding the point of inflection. Storage modulus ( $G'$ ) and loss modulus ( $G''$ ) were determined by frequency sweeps taken at 1% strain from 10 to 0.01 Hz. Unidirectional shear rate sweeps were taken from 100 to  $0.01 \text{ s}^{-1}$  by shearing the sample at a chosen shear-rate ( $\dot{\gamma}$ ) while measuring shear stress ( $\sigma$ ). An effective viscosity ( $\eta$ ) was determined from the ratio of shear-stress to shear-rate in these measurements. A linear regression was then performed to determine the zero-frequency limit and resultant yield stress of the microgel systems on GraphPad. Strain cycle and recovery experiments were conducted by alternating 1% strain for 120 s and 500% strain for 60 s over three periods at 1 Hz. A SRFS analysis was conducted to determine the yield strain rate. The strain amplitude at a given frequency was mapped against strain rate, then the yield strain rate was determined by taking the product of  $\omega$  and yield strain, where  $\omega$  is the angular frequency in  $\text{rad s}^{-1}$ . This strain rate amplitude was compared to the shear-rate range in the unidirectional shear-rate sweep to determine the accuracy of the yield stress as measured by the oscillatory strain sweeps.

**Force of Injection Measurements:** Force of injection measurements were taken using a force sensor (Tekscan, Flexiforce), Redboard (SparkFun), and syringe pump. The plunger of a Luer-lock 1 mL syringe (BD) was removed, and using a spatula, 200  $\mu\text{L}$  of microgels were loaded into the back of the syringe. The plunger was replaced, and the gels were compressed into the bore of the syringe. A 20G, 1" needle (BD Precision Glide) was connected, and the syringe was then loaded onto a syringe pump with the force sensor placed between the syringe plunger and pump actuator. The force sensor was connected to a Redboard for data acquisition. The microgels were extruded for 30 s at a volumetric flow rate of  $600 \mu\text{L min}^{-1}$ . Voltage output was recorded using Arduino IDE. The extrusion force was calculated by converting voltages to forces using a standard force–voltage calibration curve created using known weights before experimentation. The wall shear stress was determined by using the derived Navier–Stokes equations of a turbulent shear-thinning fluid through the needle of length ( $L$ ) and internal diameter ( $d$ ) due to a pressure drop ( $\Delta P$ ) within the needle for microgels and fragmented gels (Equation (2)). The pressure drop was defined as the difference between the entrance pressure applied at the plunger and the exit pressure at the needle opening.

$$\tau_w = \frac{\Delta P * R}{2L} \quad (2)$$

The wall shear stress for PBS was determined using a derivation of the Navier–Stokes Equations (Equation (3)).<sup>[43–45]</sup>

$$\tau_w = \frac{\Delta P * R}{2L} \left( -\frac{R}{2} + 1 \right) \quad (3)$$

**In Vitro Injection of Pancreatic Islets and Cells:** Jurkat T cells were added to granular hydrogels at a density of  $5 \times 10^6 \text{ cells mL}^{-1}$ . Cells and gels were mixed in 1 mL of media and then centrifuged for 5 min at  $500 \times g$  to remove supernatant and compact the scaffold. The cell + gel mixture was loaded into the syringe the same as above. The syringe was then connected to an Ibidi channel slide (Ibidi 15  $\mu\text{-Slide VI}$ ) and injected into the chip 50  $\mu\text{L}$  at a time. The cells were then labeled with Calcein AM and EthD-1 to assess viability. Each 50  $\mu\text{L}$  fraction was imaged individually as it was extruded from the needle into the channel slide. We quantified the separation of the injection fractions by counting the total number of cells injected and dividing by the number of cells quantified for each volume partition for both microspheres and fragmented gels

Human pancreatic islets from deceased nondiabetic donors were obtained from the Integrated Islet Distribution Program (IIDP) at City of Hope and Prodo Labs (Table S1, Supporting Information) and were mixed with granular hydrogels prior to injection testing. Briefly, 100  $\mu\text{L}$  of compacted granular gel was added to a 1.5 mL centrifuge tube,  $\approx 100$  pancreatic islets were hand-picked and suspended in 10  $\mu\text{L}$  of media. The islets were then pipetted into the center of the gel. The islet + gel mixture was slowly mixed by stirring the pipette tip in the gel. The islet plus gel mixture was loaded into the syringe the same as above and carefully compacted, a 20G, 1" needle was attached before injecting into an 8-well plate. Islets were labeled with Calcein AM and EthD-1 to assess viability after injection.

**Microscopy:** Microgels were imaged on a Leica SP8 confocal laser-scanning microscope using  $10\times/0.3$  and  $20\times/0.8$  numerical aperture Plan-Apochromat air objectives at  $1024 \times 1024$  pixel resolution. Images were processed and quantified using Fiji. ROIs were determined using either the analyze particle tool in ImageJ for microgel size analysis or the StarDist plug-in for cell counting in the cell and islet injections.<sup>[41,46]</sup>

**Statistical Analysis:** Means among three or more groups were compared by one-way ANOVA in GraphPad Prism 8 Software. If deemed significant, Tukey's posthoc pairwise comparisons were performed. Means between two groups were compared by a two-tailed student's  $t$ -test. A robust regression and outlier removal analysis (ROUT method) was conducted to remove outliers from rheology data. A confidence level of 95% was considered significant. The statistical test, exact  $p$  values, and definition of  $n$  are all indicated in the individual figure legends. All error bars in the figures display the mean  $\pm$  s.d.

## Supporting Information

Supporting Information is available from the Wiley Online Library or from the author.

## Acknowledgements

This work was supported by NIH grants R01DK124267 and R01DK132387 and JDRF grant 2-SRA-2019-781-S-B (E.A.P). Human pancreatic islets were provided by the NIDDK-funded Integrated Islet Distribution Program (IIDP) at the City of Hope, (grant no. 2UC4DK098085), and the JDRF-funded IIDP Islet Award Initiative. The authors thank Anton Paar for the use of the Anton Paar 702 rheometer through their VIP academic research program (T.E.A.). This material is based on work supported by the National Science Foundation under grant no. DMR-1352043 (T.E.A.).

## Conflict of Interest

The authors declare no conflict of interest.

## Author Contributions

A.E.W. performed the experiments and analyzed the data. S.D. helped perform rheological testing and analysis. T.E.A. provided access to mechanical testing instrumentation, helped perform rheological measurements, and analyzed and interpreted the rheometry data. E.A.P. conceived the project and supervised the work. A.E.W. and E.A.P. wrote the article. All authors discussed the results and commented on the manuscript.

## Data Availability Statement

The data that support the findings of this study are available from the corresponding author upon reasonable request.

## Keywords

biomaterials, guest–host, maleimide, MAP hydrogels, pancreatic islets, PEG-MAL, shear-thinning

Received: May 19, 2022

Revised: July 12, 2022

Published online:

- [1] A. C. Daly, L. Riley, T. Segura, J. A. Burdick, *Nat. Rev. Mater.* **2020**, *5*, 20.
- [2] M. H. Chen, J. J. Chung, J. E. Mealy, S. Zaman, E. C. Li, M. F. Arisi, P. Atluri, J. A. Burdick, *Macromol. Biosci.* **2019**, *19*, 1800248.
- [3] N. J. Darling, E. Sideris, N. Hamada, S. T. Carmichael, T. Segura, *Adv. Sci.* **2018**, *5*, 1801046.
- [4] N. J. Darling, W. Xi, E. Sideris, A. R. Anderson, C. Pong, S. T. Carmichael, T. Segura, *Adv. Healthcare Mater.* **2020**, *9*, 1901391.
- [5] J. E. Mealy, J. J. Chung, H.-H. Jeong, D. Issadore, D. Lee, P. Atluri, J. A. Burdick, *Adv. Mater.* **2018**, *30*, 1705912.
- [6] M. Shin, K. H. Song, J. C. Burrell, D. K. Cullen, J. A. Burdick, *Adv. Sci.* **2019**, *6*, 1901229.
- [7] Widener, A. E., M. Bhatta, T. E. Angelini, E. A. Phelps, *Biomater. Sci.* **2021**, *9*, 2480.
- [8] L. Riley, L. Schirmer, T. Segura, *Curr. Opin. Biotechnol.* **2019**, *60*, 1.
- [9] C. S. O'Bryan, T. Bhattacharjee, S. R. Niemi, S. Balachandar, N. Baldwin, S. T. Ellison, C. R. Taylor, W. G. Sawyer, T. E. Angelini, *MRS Bull.* **2017**, *42*, 571.
- [10] M. H. Chen, L. L. Wang, J. J. Chung, Y.-H. Kim, P. Atluri, J. A. Burdick, *ACS Biomater. Sci. Eng.* **2017**, *3*, 3146.
- [11] T. H. Qazi, J. A. Burdick, *Biomater. Biosyst.* **2021**, *1*, 100008.
- [12] A. Charlet, F. Bono, E. Amstad, *Chem. Sci.* **2022**, *13*, 3082.
- [13] C. L. Franco, J. Price, J. L. West, *Acta Biomater.* **2011**, *7*, 3267.
- [14] W. Leong, T. T. Lau, D.-A. Wang, *Acta Biomater.* **2013**, *9*, 6459.
- [15] T. Nisisako, T. Torii, *Lab Chip* **2008**, *8*, 287.
- [16] A. S. Caldwell, G. T. Campbell, K. M. T. Shekiri, K. S. Anseth, *Adv. Healthcare Mater.* **2017**, *6*, 1700254.
- [17] A. S. Caldwell, V. V. Rao, A. C. Golden, K. S. Anseth, *Biomaterials* **2020**, *232*, 119725.
- [18] N. A. Impellitteri, M. W. Toepke, S. K. Lan Levengood, W. L. Murphy, *Biomaterials* **2012**, *33*, 3475.
- [19] J. Chedly, S. Soares, A. Montembault, Y. Von Boxberg, M. Veron-Ravaille, C. Mouffle, M.-N. Benassy, J. Taxi, L. David, F. Nothias, *Biomaterials* **2017**, *138*, 91.
- [20] Muir, V. G., T. H. Qazi, J. Shan, J. Groll, J. A. Burdick, *ACS Biomater. Sci. Eng.* **2021**, *7*, 4269.
- [21] M. Hirsch, A. Charlet, E. Amstad, *Adv. Funct. Mater.* **2021**, *31*, 2005929.
- [22] S. H. Pun, M. E. Davis, *Bioconjugate Chem.* **2002**, *13*, 630.
- [23] J.-W. Wang, K.-X. Yu, X.-Y. Ji, H. Bai, W.-H. Zhang, X. Hu, G. Tang, *Molecules* **2021**, *26*, 2412.
- [24] S. Rezakhani, N. Gjorevski, M. P. Lutolf, *Adv. Funct. Mater.* **2020**, *30*, 2000761.
- [25] C. S. O'Bryan, C. P. Kabb, B. S. Sumerlin, T. E. Angelini, *ACS Appl. Bio Mater.* **2019**, *2*, 1509.
- [26] H. M. Wyss, K. Miyazaki, J. Mattsson, Z. Hu, D. R. Reichman, D. A. Weitz, *Phys. Rev. Lett.* **2007**, *98*, 238303.
- [27] B. J. Ballermann, A. Dardik, E. Eng, A. Liu, *Kidney Int.*, **1998**, *54*, S100.
- [28] D. J. Acheson, *Elementary Fluid Dynamics*, Oxford University Press, Oxford **1990**.
- [29] S. Priyadarshini, R. Ponalagusamy, *Appl. Bionics Biomech.* **2015**, *2015*, 1.
- [30] T. H. Qazi, J. Wu, V. G. Muir, S. Weintraub, S. E. Gullbrand, D. Lee, D. Issadore, J. A. Burdick, *Adv. Mater.* **2022**, *34*, 2109194.
- [31] A. Ellis, J. C. Jacquier, *J. Food Eng.* **2009**, *90*, 141.
- [32] S. J. Stubbley, O. J. Cayre, B. S. Murray, I. C. Torres, I. F. Farrés, *Food Hydrocolloids* **2021**, *121*, 107045.
- [33] T. J. Hinton, Q. Jallerat, R. N. Palchesko, J. H. Park, M. S. Grodzicki, H.-J. Shue, M. H. Ramadan, A. R. Hudson, A. W. Feinberg, *Sci. Adv.* **2015**, *1*, e1500758.
- [34] V. G. Muir, T. H. Qazi, S. Weintraub, B. O. Torres Maldonado, P. E. Arratia, J. A. Burdick, *Small* **2022**, <https://doi.org/10.1002/smll.202201115>.
- [35] X.-H. Qin, K. Labuda, J. Chen, V. Hruschka, A. Khadem, R. Liska, H. Redl, P. Slezak, *Adv. Funct. Mater.* **2015**, *25*, 6606.
- [36] M. Guvendiren, H. D. Lu, J. A. Burdick, *Soft Matter* **2012**, *8*, 260.
- [37] C. B. Highley, K. H. Song, A. C. Daly, J. A. Burdick, *Adv. Sci.* **2019**, *6*, 1801076.
- [38] C. Loebel, C. B. Rodell, M. H. Chen, J. A. Burdick, *Nat. Protoc.* **2017**, *12*, 1521.
- [39] T. Binaree, E. Azéma, N. Estrada, M. Renouf, I. Preechawuttipong, *Phys. Rev. E* **2020**, *102*, 022901.
- [40] N. J. Darling, Y.-S. Hung, S. Sharma, T. Segura, *Biomaterials* **2016**, *107*, 199.
- [41] J. Schindelin, I. Arganda-Carreras, E. Frise, V. Kaynig, M. Longair, T. Pietzsch, S. Preibisch, C. Rueden, S. Saalfeld, B. Schmid, J.-Y. Tinevez, D. J. White, V. Hartenstein, K. Eliceiri, P. Tomancak, A. Cardona, *Nat. Methods* **2012**, *9*, 676.
- [42] S. Karmakar, *Recent Trends in Materials Physics and Chemistry*, Studium Press (India) Pvt. Ltd., India **2019**, p. 117–159.
- [43] B. A. Aguado, W. Mulyasmita, J. Su, K. J. Lampe, S. C. Heilshorn, *Tissue Eng. Part A* **2012**, *18*, 806.
- [44] T. A. Becker, D. R. Kipke, *J. Biomed. Mater. Res.* **2002**, *61*, 533.
- [45] J. F. Steffe, *Rheological Methods in Food Process Engineering*, 2nd ed., Freeman Press, East Lansing, MI, USA **1996**.
- [46] U. Schmidt, M. Weigert, C. Broaddus, G. Myers, *Cell Detection with Star-Convex Polygons* (Eds: A. Frangi, J. Schnabel, C. Davatzikos, C. Alberola-López, G. Fichtinger), Lecture Notes in Computer Science (LNIP), Vol. 11071, Springer, Cham, Switzerland **2018**, p. 265–273.